Please cite this article in press as: Taylor et al., Simulation of receptor triggering by kinetic segregation shows role of oligomers and close contacts, Biophysical Journal (2022), https://doi.org/10.1016/j.bpj.2022.03.033

Biophysical *Journal*
Article

Biophysical Society

Simulation of receptor triggering by kinetic segregation shows role of oligomers and close contacts

Robert Taylor,[1] Jun Allard,[1,2,3] and Elizabeth L. Read[3,4,*]
[1]Department of Physics & Astronomy, University of California, Irvine; [2]Department of Mathematics, University of California, Irvine; [3]Center for Complex Biological Systems, University of California, Irvine; and [4]Department of Chemical & Biomolecular Engineering, University of California, Irvine

ABSTRACT The activation of T cells, key players of the immune system, involves local evacuation of phosphatase CD45 from a region of the T cell's surface, segregating it from the T cell receptor. What drives this evacuation? In the presence of antigen, what ensures evacuation happens in the subsecond timescales necessary to initiate signaling? In the absence of antigen, what mechanisms ensure that evacuation does not happen spontaneously, which could cause signaling errors? Phenomena known to influence spatial organization of CD45 or similar surface molecules include diffusive motion in the lipid bilayer, oligomerization reactions, and mechanical compression against a nearby surface, such as that of the cell presenting the antigen. Computer simulations can investigate hypothesized spatiotemporal mechanisms of T cell signaling. The challenge to computational studies of evacuation is that the base process, spontaneous evacuation by simple diffusion, is in the extreme rare event limit, meaning direct stochastic simulation is unfeasible. Here, we combine particle-based spatial stochastic simulation with the weighted ensemble method for rare events to compute the mean first passage time for cell surface availability by surface reorganization of CD45. We confirm mathematical estimates that, at physiological concentrations, spontaneous evacuation is extremely rare, roughly 300 years. We find that dimerization decreases the time required for evacuation. A weak bimolecular interaction (dissociation constant estimate 460 μM) is sufficient for an order of magnitude reduction of spontaneous evacuation times, and oligomerization to hexamers reduces times to below 1 s. This introduces a mechanism whereby externally induced CD45 oligomerization could significantly modify T cell function. For large regions of close contact, such as those induced by large microvilli, molecular size and compressibility imply a nonzero reentry probability of 60%, decreasing evacuation times. Simulations show that these reduced evacuation times are still unrealistically long (even with a fourfold variation centered around previous estimates of parameters), suggesting that a yet-to-be-described mechanism, besides compressional exclusion at a close contact, drives evacuation.

SIGNIFICANCE In the immune system, T cell sensing of pathogens depends on a process called T cell receptor triggering. In this process, proteins on the cell surface undergo reorganization, including local depletion of large membrane proteins from the area surrounding the T cell receptor. Computer simulations of protein dynamics provide a means to investigate phenomena in greater detail than that afforded by experiments. However, even simulations present challenges, because tracking the motion and interactions of individual molecules is computationally expensive. Combining a rare event algorithm with spatial simulations, we show that biochemical and mechanical properties drastically affect depletion timescales, and thus receptor triggering. Quantitative understanding of these timescales will constrain hypothesized mechanistic models and could suggest new strategies for T cell engineering.

INTRODUCTION

In a T cell-mediated immune response, T cells sense pathogens through the interaction of T cell receptors (TCRs) with antigens presented on the surface of nearby cells (shown schematically in Fig. 1 *A*, *left*). In a key step known as TCR triggering, this binding interaction triggers an intracellular signaling cascade. The physical and biochemical mechanisms of TCR triggering are not fully understood. A number of different models have been proposed (reviewed in (1,2)). These models synthesize a variety of experimental observations, and they help to further understanding of how T cells can achieve exquisite sensitivity to small amounts of antigens, while also discriminating antigens.

Submitted November 30, 2021, and accepted for publication March 28, 2022.

*Correspondence: elread@uci.edu

Editor: Alexander Fletcher.

https://doi.org/10.1016/j.bpj.2022.03.033

Please cite this article in press as: Taylor et al., Simulation of receptor triggering by kinetic segregation shows role of oligomers and close contacts, Biophysical Journal (2022), https://doi.org/10.1016/j.bpj.2022.03.033

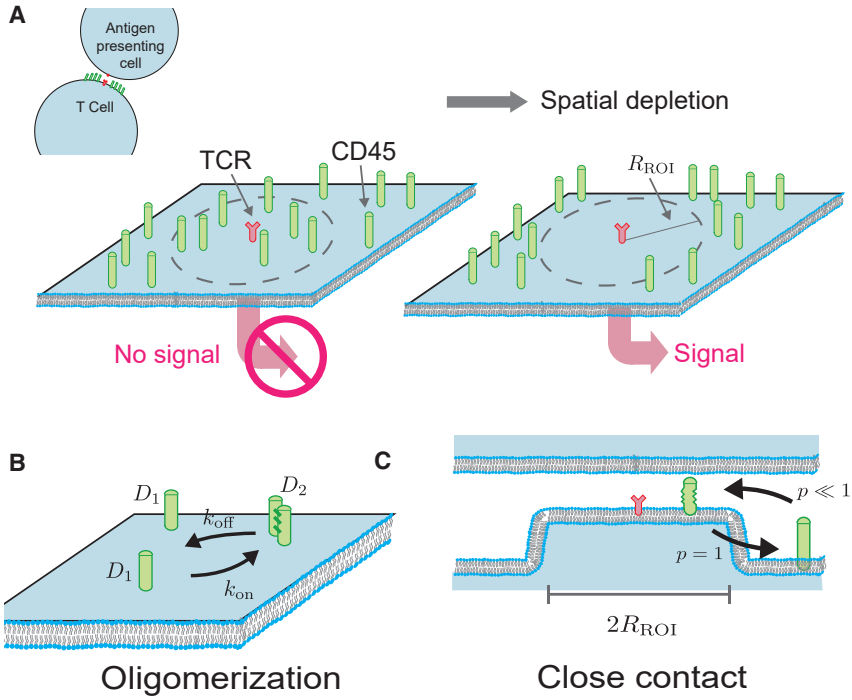

FIGURE 1 Surface dynamics for a large, membrane-bound surface molecule such as CD45. (*A*) T cell receptor (TCR) binding to an antigen presented by another cell. Left: if CD45 is uniformly distributed around the receptor, signaling is inhibited. Right: the local depletion of CD45 from the region of interest (ROI) near the receptor, approximated here as a circle with radius R_{ROI}, is a key step in TCR signaling (1,2). (*B*) Intermolecular interactions between CD45, e.g., oligomerization of CD45 into dimers. Diffusion coefficients for monomers and dimers are D_1 and D_2, respectively (13,14). (*C*) Close contacts created by, e.g., microvilli, could lead to biased movement of CD45 due to compressional resistance of the molecule (15). We represent these close contacts by probabilistically limiting entry into the ROI. To see this figure in color, go online.

TCR triggering is associated with reorganization of cell surface proteins, shown schematically in Fig. 1 *A*. Local depletion of surface proteins from the area surrounding the receptor—in particular, the large ectodomain protein phosphatases, CD45 and CD148—has been demonstrated to be an important step (3,4). This depletion is consistent with a model of T cell triggering known as the kinetic segregation model (1). In this model, large ectodomain proteins segregate from the region of close cell-cell contact that forms when the TCR binds to antigens presented on a neighboring cell. Depletion of these phosphatases from the receptor's vicinity prevents them from interfering with stable phosphorylation of the TCR's cytoplasmic domains. That is, this depletion prevents the phosphatases from interfering with initiation of the signaling cascade that ultimately leads to activation of the T cell.

The kinetic segregation model is supported by various lines of evidence: CD45 has been shown to have an inhibitory effect on receptor triggering (5,6) and is found in low concentrations close to triggered receptors (6,7), and synthetically holding a receptor in the CD45 depletion region augments signaling (8). The model is also consistent with the known geometry of the rigid extracellular domain of CD45, ~21 nm in length (7,9), which is larger than the distance spanned by the receptor-antigen complex (~13 nm) (7,10). However, the kinetic segregation model cannot by itself fully explain TCR triggering: other mechanisms likely contribute (e.g., see (1)), and CD45 plays somewhat contradictory roles (5).

How and when the local depletion (also hereon termed *evacuation*) of large ectodomain phosphatases from the receptor vicinity occurs remains unclear. It could happen pre-contact formation (e.g., does local evacuation of CD45 clear the way for receptor-antigen binding?) or post close contact formation (e.g., a scenario where receptor-antigen binding is first enabled by close contact due to a microvillus (11), or active membrane protrusion). The question of what drives this evacuation can be cast in three different lights: in the absence of receptor ligation, what mechanisms ensure that evacuation does not happen accidentally? In the presence of ligation, what ensures that evacuation happens in subsecond timescales necessary to initiate and sustain a signal? Finally, if the process of evacuation tips the balance from inhibitory to stimulatory signaling in T cells, could modulating the evacuation process itself be an avenue accessible to engineered therapeutics?

Various mechanisms for this evacuation process have been proposed, and there is no scientific consensus on which are likely to be most important. These include: simple Brownian motion of CD45 in the plasma membrane (12), oligomerization reactions between the molecules (13,14) shown schematically in Fig. 1 *B*, and mechanical compression by a nearby surface, such as that of the cell presenting the antigen. The compression region can be conceptually categorized as either a close contact of ~100 nm (15,16), shown schematically in Fig. 1 *C*, where there is no net lateral pressure on the molecules within the close contact, or something more similar to the wedge or tent shape resulting from a force on a single receptor pulling the membrane

Please cite this article in press as: Taylor et al., Simulation of receptor triggering by kinetic segregation shows role of oligomers and close contacts, Biophysical Journal (2022), https://doi.org/10.1016/j.bpj.2022.03.033

at a point (17). The latter case has been studied theoretically (17,18). Beyond the scope explored in this work, there are many more possible mechanisms, including spatial heterogeneity due to lipid composition, interaction with the cytoskeleton (19–21), or crowding out by CD3 (22). Also, modulation of the configurational state of the individual molecules themselves can modulate their organization, e.g., by electrostatic interaction with the lipid membrane (23,24).

Computer simulations of the spatiotemporal events involved in receptor triggering and immune synapse formation can provide a means to investigate phenomena that lie beyond the spatiotemporal resolution of measurement techniques (25). More generally, computational modeling is useful for formalizing assumptions, isolating the effects of individual parameters, and uncovering new phenomena (among other purposes, reviewed in (26)). In this paper, we investigate the evacuation process through computer simulations tracking reaction-diffusion dynamics of protein molecules on the cell surface. To simulate wide ranges of parameters, including different molecular phenomena, with a physiological and near-physiological numbers of molecules, we made recourse to the weighted ensemble algorithm (27), an enhanced sampling simulation method.

The paper is outlined as follows. We first describe the rare event reaction-diffusion framework. We use this to confirm previous mathematical estimates that, at physiological concentrations, spontaneous evacuation is extremely rare (12). Following that, in "oligomerization" we explore the implications of molecular interactions between the surface molecules. We find that dimerization decreases the timescale of evacuation for even weak bimolecular interaction by several orders of magnitude. The formation of higher-order oligomers reduces evacuation to a subsecond process, opening the possibility that an engineered oligomer of CD45 could significantly modulate receptor triggering. In "close contacts," we simulate the motion of surface molecules in and around a region where the membrane is near another surface, and molecules in this region are compressed. We find that formation of close contacts also decreases the timescale of evacuation. However, for large regions of close contact, such as those induced by large microvilli, our model predicts evacuation times that are still too long by several orders of magnitude, using current estimates for the molecular size and compressibility of CD45. This suggests that the change in molecular motion driven by close contact alone is not sufficient to drive receptor triggering.

RESULTS

A rare event reaction-diffusion simulation

Molecules in our model are represented as individual particles moving on a two-dimensional (2D) surface. Their mean density is ρ, and we assume there is a region of interest (ROI), for example, near a single TCR, that we approximate as a disk with radius R_{ROI}. We make the simplifying assumption that the receptor motion is negligible relative to the motion of the individual CD45 molecules. The ROI lies in the center of a 2D square domain with edge length L. The quantity we wish to compute is the mean time until the ROI is empty—which we refer to as the evacuation time or mean first passage time (MFPT) —under various assumptions about the dynamics of the molecules. In the base case, we assume that motion is purely diffusive with coefficient D (which could be thermal or include active, random forces (28)). Note that previous work (12) has shown that diffusion alone is too slow to be consistent with experimental data, giving MFPTs of $\sim 10^{10}$, whereas triggering can occur in reality within seconds (29,30). That is, the simultaneous evacuation of all molecules from the ROI by simple diffusion, given physiological surface density and ROI size, is a rare event. We are interested in the rare event limit because, first, its quantification helps reject this null hypothesis, and, second, it provides a necessary starting point for hypothesizing what may accelerate the biological process of T cell activation out of the rare event limit.

Summary of key parameters in the base model

We parameterize our model based on experiment-derived estimates. The key parameters of the base model are the size of the evacuation region, the diffusion coefficient of CD45, and the surface density of CD45. The size of the evacuation region (that is, the radius of the ROI) provides a characteristic length scale for the model system. Assuming $R_{ROI} = 100$ nm (15,17,31), and assuming the diffusion coefficient to be $D = 0.01\ \mu m^2/s$ (32), these provide a characteristic timescale for the system of $R^2_{ROI}/D \approx 1$ s. We define scaled units for molecule density, ρ, as molecules per R^2_{ROI}. In these scaled units, we estimate the physiological surface density of CD45 to be $\rho \approx 9$ molecules per R^2_{ROI}(17). Parameters are listed in Table S1; further details of parameter values are discussed in Methods.

Combining weighted ensemble (WE) and Smoldyn allows simulation of long timescale stochastic spatial phenomena.

To simulate evacuation in the rare event limit, we combine the particle-based reaction-diffusion simulator Smoldyn (33) with a weighted ensemble algorithm (27,34–36). The algorithm has been shown to be statistically exact for many stochastic processes (35) and has been applied to many systems, especially in molecular dynamics (37). In this algorithm, shown schematically in Fig. 2, many Smoldyn simulations are run in parallel, each assigned a weight w_i, with $\sum_i w_i = 1$. An order parameter is used (here, the number of particles in the ROI, n_{in}) to bin the state space (Fig. 2 *A*). Periodic redistribution of weights and trajectories among the bins occurs after each time interval τ. More simulations are run in probabilistically less-likely

Please cite this article in press as: Taylor et al., Simulation of receptor triggering by kinetic segregation shows role of oligomers and close contacts, Biophysical Journal (2022), https://doi.org/10.1016/j.bpj.2022.03.033

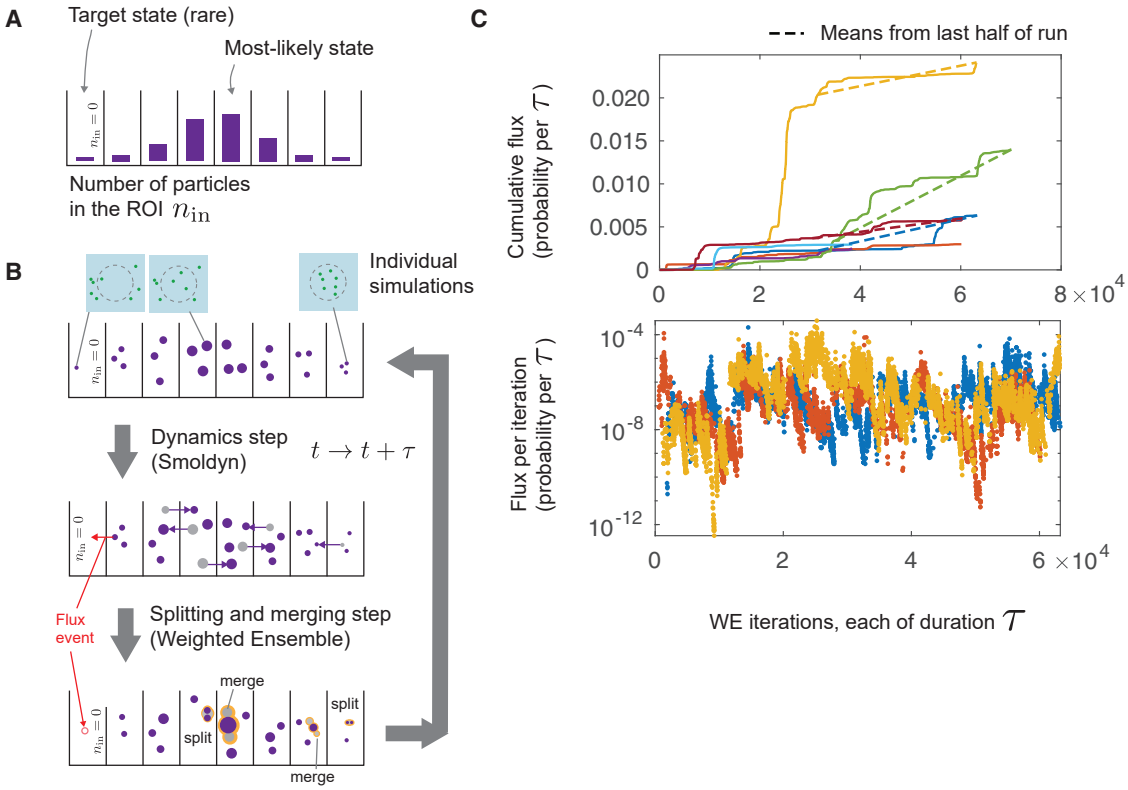

FIGURE 2 Weighted ensemble algorithm with Smoldyn spatial dynamics simulations. (*A*) Partitioning of simulation state space into bins based on the number of molecules in the ROI, $0 \langle n_{in} \langle N$, where N is the total number of molecules. Bar heights represent the relative probability of the system to be found in the corresponding bin at equilibrium. In the simplest case in which molecules experience diffusion-only dynamics, this is a binomial distribution. (*B*) Description of the algorithm. Individual simulations (replicas) are shown as purple circles, and have statistical weights that can vary from replica to replica, represented here through circle size. Simulations are allowed to propagate according to dynamics simulated by the dynamics engine Smoldyn (33) for a period of time τ. After the dynamics step has completed, the replicas are reexamined to see their new bin locations. The number of replicas in each bin is then compared with m_{targ}, the desired number of replicas in each bin. Bins with more than m_{targ} replicas have a "merging" event, where the replicas with the smallest individual weights are removed and their weight is redistributed to another replica within the same bin. Bins with fewer than m_{targ} (but still ›0) replicas have "splitting" events where the replicas with the most weight are duplicated into two daughter replicas, with the weight from the parent being redistributed equally to the daughters. Flux events, representing complete evacuations of the ROI (*red*) have their replicas deleted and weight redistributed to replicas outside of the flux bin. For details on this redistribution of weights from flux events, see Fig. S1. (*C*) Flux measurements from multiple, independent runs displayed in two different ways: total flux accumulated (top, *y* axis scaled linearly) and flux accumulated per weighted ensemble (WE) iteration (bottom, *y* axis scaled logarithmically; fewer runs shown for clarity). For each WE run, the measurements in the first half of the run are discarded to exclude the fluxes that might be measured during weight redistribution between the initial simulation state and the simulation state after many WE steps have passed. The mean fluxes measured during this period from multiple independent runs (*slopes of dashed lines*) are then used to estimate the mean first passage time to the evacuated state. Cumulative fluxes for seven runs are shown in the top figure, with the time series for three of those runs being shown in the bottom plot. Since the bottom plot is on a logarithmic scale, WE iterations where no flux was measured (in this case, ~90% of iterations) do not appear. To see this figure in color, go online.

regions of state space, but assigned a smaller weight. This focuses computational power on rare events while still maintaining an algorithmically exact statistical ensemble (35,37). Every τ time units, we record the probability flux into the evacuated state (i.e., the summed weights of trajectories that reached the bin with $n_{in} = 0$ during that time interval), as shown schematically by red arrows and circles in Fig. 2 *B*, and actual evacuated weights shown in Fig. 2 *C*. Trajectories that reach evacuation are killed, and their weights are redistributed into the system. Once the system reaches steady state, the mean flux gives the reciprocal of the MFPT (34). In practice, an estimate of the MFPT is obtained based on multiple independent simulations, as indicated by different colored lines in Fig. 2 *C*. For full details see Methods and Fig.S1. We name this algorithm and combination WE-Smoldyn.

A summary of WE and simulation hyperparameters is given in Table S1.

WE-Smoldyn agrees with brute force stochastic simulation at low densities and approaches asymptotic calculation for high densities.

We first simulate evacuation for a density of particles ρ undergoing diffusion only, and compute the mean time to evacuation. In Fig. 3 *A*, we demonstrate the computational ability to simulate evacuation and compute MFPTs for a range of surface density values, reaching $\rho = 10$, which is consistent with experimental estimates (15,17) and which corresponds to a mean number inside the ROI of $\overline{n_{in}} = \pi\rho = 31$. The

Please cite this article in press as: Taylor et al., Simulation of receptor triggering by kinetic segregation shows role of oligomers and close contacts, Biophysical Journal (2022), https://doi.org/10.1016/j.bpj.2022.03.033

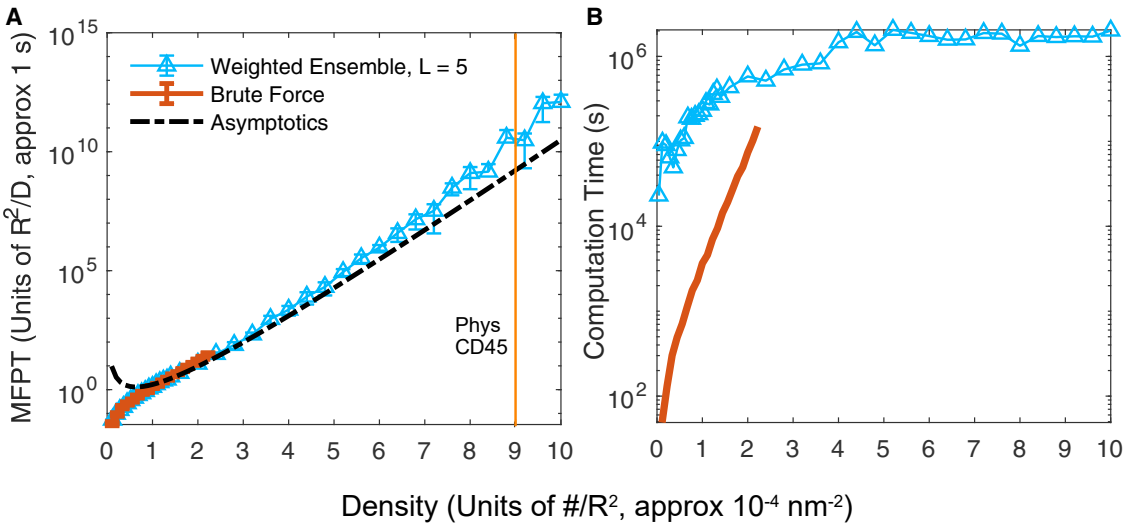

FIGURE 3 Mean evacuation time from the ROI for molecules only experiencing diffusion shows evacuation times well outside the experimentally observed timescales at physiological densities. Despite this drastic increase in evacuation times, use of weighted ensemble (WE) allows calculation on computationally feasible timescales. (*A*) Evacuation times for densities ranging up to $\rho = 10$ molecules per R_{ROI}^2. Estimate of physiological density of CD45 assuming an ROI of ~100 nm in radius and $\sim 9 \times 10^{-4}$ molecules per nm^2 (see main text) marked with a vertical line. Evacuation times from WE for domain size $L = 5$ (*blue*) agree with brute force simulations (*red*) at low ρ and with an asymptotic (infinite domain) approximation at low to intermediate ρ (12). (The asymptotics overestimate evacuation times for both methods at very low ρ). Each WE data point uses ten independent runs. Error bars for WE runs are computed by taking the average flux measured from the second half of each WE run as a single measurement, computing the 95% confidence interval of these flux measurements, and propagating these errors. Brute force error bars come from the standard error of the mean for 1000 runs. (*B*) Total computational costs for the data points in (*A*). WE data points come from summing the computation time of ten independent WE simulations, with $m_{\mathrm{targ}} = 100$ replicas per bin. WE runs were programmed to run until flux measurements from the final one-third of WE iterations and the middle one-third of WE met the following criteria: 1) nonzero flux measurements in each third numbered at least 500; 2) the KS-statistic between the two-thirds reached a value of 0.02 or lower; and 3) the KS statistic between the two-thirds with zeros removed reached a value of 0.3 or lower. Oftentimes, one or more of these requirements would not be met before reaching computation limits of an individual run, and in that case WE simulation would automatically stop after 2.5 days of computational time spent on WE and Smoldyn dynamics. Brute force data points come from summing the computation time of 1000 independent brute force evacuation events. WE simulations used reweighting method 2 for $\rho \leq 1$ and reweighting method 1 for $\rho \rangle 1$ (see Fig. S1). Parameters were $\tau = 50\Delta t$, $m_{\mathrm{targ}} = 100$, $\Delta t = 10^{-6}$. To see this figure in color, go online.

MFPT grows superexponentially with ρ, reaching $\mathrm{T} \approx 10^{12}$ s at the highest simulated density. The MFPT has an uncertainty of less than one order of magnitude (error bars are standard error of the mean).

To validate our method, we compare it with a brute force simulation using Smoldyn at low ρ (red). At high ρ, we compare it with the asymptotic approximation from (12) (black dashed), which gives the following value for the MFPT.

$$T = \frac{k_{2\mathrm{D}} R_{\mathrm{ROI}}^2 e^{\overline{n_{\mathrm{in}}}}}{D \overline{n_{\mathrm{in}}}^2}, \quad \overline{n_{\mathrm{in}}} \gg 1. \tag{1}$$

Here, $k_{2\mathrm{D}} \approx 0.7$ is a constant independent of all parameters (see (12)). In the rare event limit, agreement to the asymptotics is within two orders of magnitude, and we hypothesized that the disagreement is due to a finite domain size in our simulation (whereas the asymptotic approximation is in the limit of infinite domain). We confirm that the MFPT, estimated from our simulations as a function of increasing domain size, approaches the value in Eq. 1 (see Fig. S2). The domain size effect can be intuitively understood to result from the difference in particle distributions for a small domain versus a large domain during an evacuation event. For evacuation to occur, the density of particles outside the ROI must increase, while the density of particles inside the ROI must decrease (to zero). Also, the ROI area makes up a greater fraction of the total system area for a small domain, as compared with a large domain. Therefore, more particles must be "squeezed" into a smaller area (that is, the density of particles outside the ROI must increase further from the equilibrium value) for evacuation to occur in the small domain case, as compared with the large domain.

The computational scaling in Fig. 3 *B* suggests that simple time stepping would take 4×10^5 years of CPU time for 1000 evacuation events, whereas the WE method took approximately 25 days per MFPT measurement (2.5 days per measurement, then repeated 10 times) on a single CPU core. Thus, the simulations we present throughout this paper would be unfeasible without recourse to an enhanced sampling algorithm such as WE.

The definition of evacuation time we use here and in (12) is instantaneous, in other words until the last molecule reaches the boundary of the ROI. This raises two notes: first, this is an approximation, since in the T cell it is likely that

Please cite this article in press as: Taylor et al., Simulation of receptor triggering by kinetic segregation shows role of oligomers and close contacts, Biophysical Journal (2022), https://doi.org/10.1016/j.bpj.2022.03.033

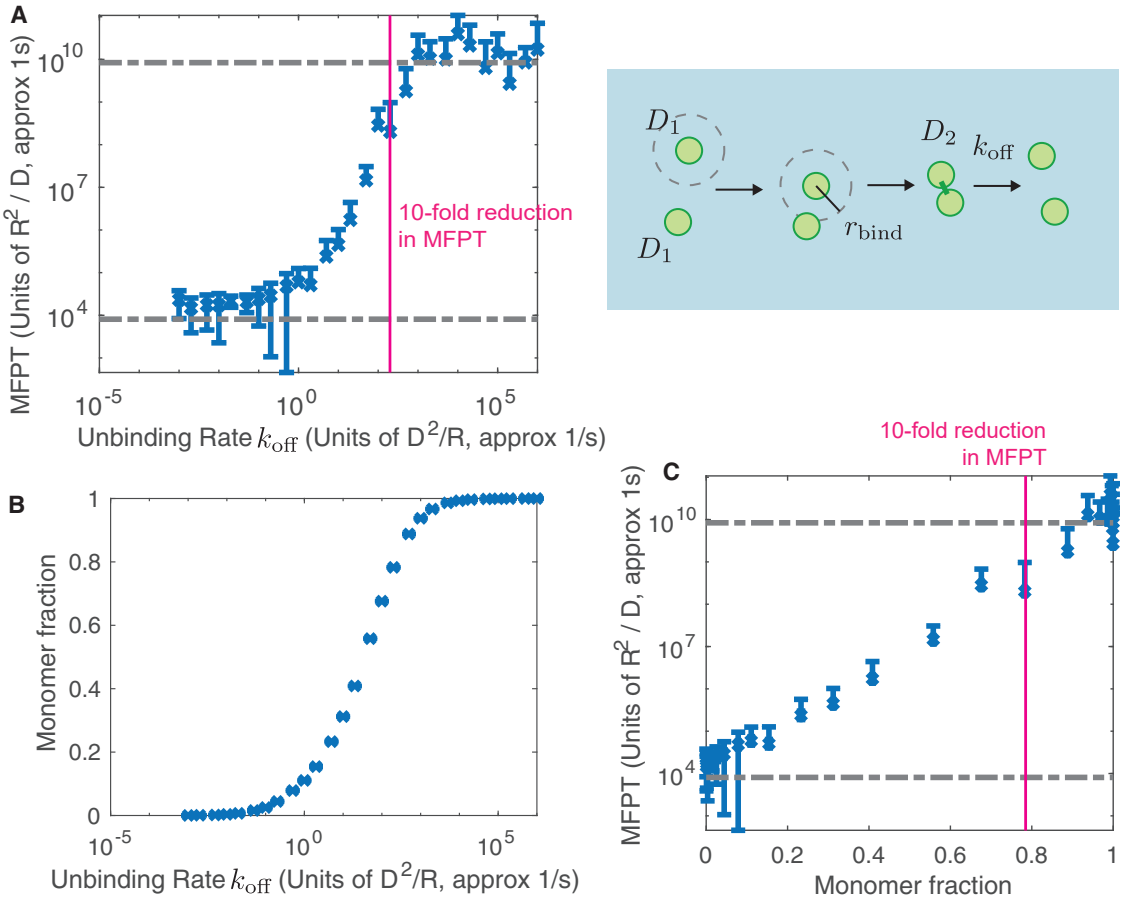

FIGURE 4 Dimerization of evacuating molecules causes several-order reduction in evacuation time (MFPT). (*A*) Right: schematic of dimerization model used in Smoldyn. Molecules, diffusing at a rate D_1, which get within a certain distance, $r_{\text{bind}} = 0.001$, of each other combine into a dimer that diffuses at a rate of $D_2 = D_1/2$. These dimers have an unbinding rate, k_{off}, which varies across simulations. Left: reduction in unbinding rate k_{off} (moving right-to-left on axes) leads to several-order reduction in evacuation time. At low dimerization fraction (high k_{off}), evacuation time is the same as for noninteracting diffusing molecules with $\rho = 9, D = D_1$, shown by the upper dashed line. At high dimerization fraction (low k_{off}), evacuation time is the same as for noninteracting particles but with half the density and half the diffusion coefficient, i.e., $\rho = 4.5, D = D_2$. (*B*) Average monomer fraction for the simulations given in (*A*) versus k_{off}. (*C*) Same data as (*A*) and (*B*) showing the relationship between monomer fraction and evacuation time. A 10-fold reduction in evacuation time (*vertical line* in (*A*) and (*C*)) occurs when only 20% of the individual molecules are in a dimer, suggesting that even weak binding can have drastic impacts on evacuation events. To see this figure in color, go online.

a TCR in an almost-evacuated ROI could still become triggered, just at a lower rate. Second, the time-stepping algorithm we use here could lead to overestimates of the MFPT. To control for this second approximation, we confirm in Fig. S2 that MFPTs are independent of simulation time step Δt.

Oligomerization

Model for intermolecular interactions

There is some evidence that CD45 dimerizes (13,14). In this section, we explore the impact this would have on the evacuation process. To include dimerization, we add a reversible binding reaction to the model, with unbinding rate k_{off}, and binding occurring whenever two particles are within a distance $\gamma_{\text{bind}} = 10^{-2}$, which corresponds to a physical distance of 1 nm. Binding distance roughly corresponds to a binding rate. See Fig. S3 and Methods for details on simulation of reversible dimerization of surface molecules. We further assume that dimers diffuse more slowly by twofold (38). We explore the effect of varying k_{off}, i.e., of varying the equilibrium constant for the dimerization reaction.

Dimerization decreases the timescale of evacuation by orders of magnitude even for weak bimolecular interaction strengths

At low k_{off}, evacuation times are decreased by over five orders of magnitude, as shown in Fig. 4 *A* (*toward left of horizontal axis*). Order of magnitude changes in MFPT appear to track closely with corresponding steady-state monomer fractions as a function of k_{off} (Fig. 4 *B*). We can understand this heuristically as follows, making use of the asymptotic approximation (for monomer evacuation) in Eq. 1 (12). At low k_{off}, most molecules are in dimer form. Evacuation is

Please cite this article in press as: Taylor et al., Simulation of receptor triggering by kinetic segregation shows role of oligomers and close contacts, Biophysical Journal (2022), https://doi.org/10.1016/j.bpj.2022.03.033

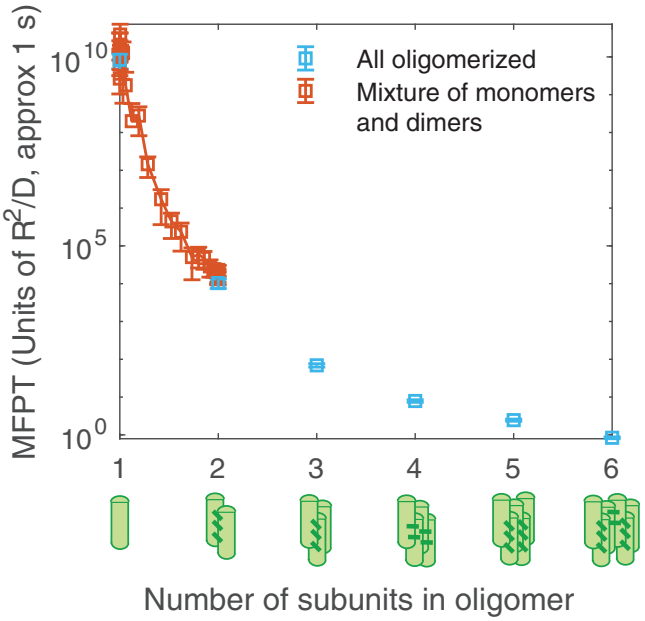

FIGURE 5 Formation of higher-order oligomers further reduces evacuation time, including times below ~1 s for hexamers. Assuming that high-affinity (e.g., low k_{off}) oligomerization would lead to a homogenous ensemble of oligomers of a particular size (*horizontal axis*), oligomer diffusion coefficients were taken to scale reciprocally with the number of subunits $D_n = D_1/n$ (38). Intermediate affinity oligomerization (*red*) would lead to heterogeneous monomeric and dimeric mixtures. We compute these intermediate evacuation times from dimerization data in Fig. 4 and Eq. 2. To see this figure in color, go online.

nominally slowed by the reduction in diffusion coefficient, since the evacuation timescales as $T = \alpha D^{-1}$ in the asymptotic (infinite domain) limit. However, this effect is outweighed by the reduction in the number of independent particles, since $T = \alpha e^N/N^2$, which leads to an almost exponentially lower MFPT (12). Thus, the linear reduction in diffusion coefficient is dominated by the near-exponential dependence on the (linear) reduction in number of particles. Indeed when we compute MFPT as a function of the fraction of monomers in Fig. 4 *C*, we observe an approximately exponential relationship.

More surprisingly, this dramatic reduction in evacuation time occurs even for weak dimerization. When monomer fraction is as high as 80%, meaning only 20% of CD45 subunits are in dimers, the MFPT is already reduced by 10-fold.

These relatively high unbinding rates correspond to weak homodimerization affinities. We can compute an effective 2D dissociation constant, defined as the concentration of reactants at which half the reactants are in the product (dimer). We find that a reaction with $k_D^{2D} = 0.0058\ nm^{-2}$ would yield a 10-fold reduction in evacuation time. A reaction with $k_D^{2D} = 0.0009\ nm^{-2}$ would yield a 1000-fold reduction. Conversion of 2D chemical properties to the equivalent 3D properties is nontrivial (39,40), but a lower-bound estimate can be obtained by dividing the 2D density by the confinement height of the reaction (39,41,42). In this case, the upper bound for the confinement height is the height of CD45 (9). Using this, we can compute a lower-bound affinity for 10-fold reduction of MFPT, $k_D^{3D} = 460\ \mu M$, which corresponds to a standard binding free energy of $\Delta G_{bind} = k_B T \ln K_D^{3D} = -19\ kJ/mol$. These binding strengths are an order of magnitude weaker than those measured for agonist TCR-peptide-MHC (43). Note that these overestimate the needed strength, since the confinement length we assumed to convert to a 3D affinity is an overestimate.

Effects of higher-order oligomers on evacuation

This led us to wonder how evacuation times would be affected by the formation of higher-order complex molecular assemblies; for example, as could be engineered using extracellular molecular linkers.

Full simulation of higher-order oligomerization was beyond our limits due to the combinatorial complexity of the number of molecular species and reactions between these. (This is algorithmically feasible, especially with rule-based modeling tools (44,45) but would be difficult to parameterize, i.e., we would either need to estimate or explore a combinatorially large number of rate constants.) However, we can use WE to compute the evacuation time assuming that k_{off} is sufficiently low, such that all molecules are in the highest-order oligomer (as shown in Fig. 5). Here, again, we assume that the diffusion coefficient is reduced proportional to the number of subunits in the complex.

For oligomers larger than dimers, we assume that the ensemble is homogenous and only made of the largest complex. Between oligomer size 1 and 2, we show heterogeneous mixtures using the same sweep of k_{off} from Fig. 4, but plotted as a function of the average number of subunits in each independently diffusing particle,

$$\text{Avg.\# subunits} = \frac{2[\#\ \text{dimers}] + [\#\ \text{monomers}]}{[\#\ \text{dimers}] + [\#\ \text{monomers}]}. \quad (2)$$

Consistent with the result for dimers, these larger oligomers evacuate faster, despite diffusing more slowly. Indeed, hexamers with strong binding evacuate within 1 s.

We have assumed that the diffusion coefficient of oligomers is $D_n = D_1/n$, where n is the number of subunits. Note that for a single molecule with a transmembrane domain, or multiple transmembrane domains very close together, previous findings suggest a linear decrease in D with lateral radius of the diffusing membrane protein (46), while other studies found that D depends more weakly on protein radius (47), and it has also been shown that the size-dependent decrease in D of membrane proteins depends on factors such as membrane crowding (48). In our case, we assume that the oligomers result from the attachment of multiple molecules each with a single transmembrane domain of unchanged size. So, the transmembrane domains are further apart than in (46–48), and therefore

Please cite this article in press as: Taylor et al., Simulation of receptor triggering by kinetic segregation shows role of oligomers and close contacts, Biophysical Journal (2022), https://doi.org/10.1016/j.bpj.2022.03.033

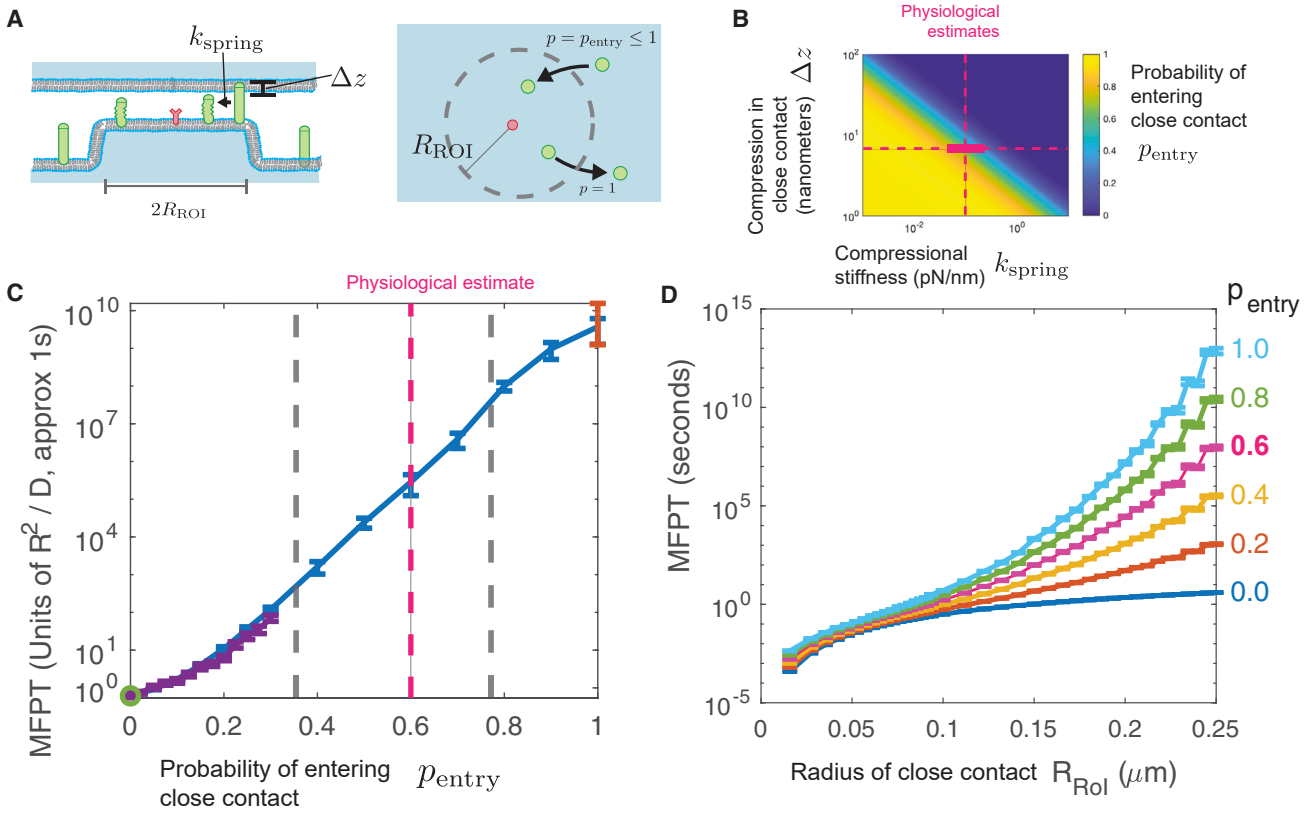

FIGURE 6 Formation of close contacts creates an energetic barrier for entry into the ROI. Even moderate energy barriers can create order of magnitude reduction in evacuation time at physiological densities. (*A*) Schematic of close contacts and how we chose to model them in Smoldyn. Close contacts, such as those from microvilli, can cause compression of large transmembrane particles, such as CD45. The energy associated with this compression is modeled as a compressed spring $E_{spring} = \frac{1}{2} k\Delta z^2$, where k is the compressional spring constant, and Δz is the distance of compression. This leads to dynamics in which movement into the ROI is reduced. We model the reduction as a probability *pentry* from the thermodynamic relation Eq. 3. (*B*) Heatmap of *pentry* for a variety of compressional stiffnesses k_{spring} and the compression size Δz. Pink dashed lines represent physiological estimates of both. The solid pink rectangle represents twofold increase and decrease of k_{spring}. (*C*) Evacuation time (MFPT) versus *pentry*, with the physiological estimate for *pentry* given by the vertical dashed, pink line. Included are results from WE simulations (*blue*) or brute force simulations (*purple*). At *pentry* = 1, we include the diffusion-only simulation result from Fig. 3 (*red*). At *pentry* = 0, we compute an analytic expression for the MFPT in Eq. 34 (supporting material) and Fig. S4, shown here in green. The inset shows, with a linear *y* axis, close agreement between brute force and WE for *pentry* ‹ 0.1. For WE runs, an alternative method of redistributing weight in the flux bin is used (see Fig. S1). Gray dashed lines show *pentry* and MFPT if the spring constant were increased or decreased by twofold. (*D*) Evacuation time versus radius of close contact, R_{ROI}, rescaled to physical units (s, μm) to show the impact of physical parameters, assuming the ansatz Eq. 4. Here, we use lower density of CD45 of 160 μm^{-2} (lower than central estimate used elsewhere) to achieve simulation at larger ROIs. To see this figure in color, go online.

hydrodynamic interactions between the transmembrane domains are weaker. Previous studies suggest that, if separated by the size of a protein, the hydrodynamic interactions are weak and the scaling of drag coefficient with n becomes linear (38). Nonetheless, our assumption of $D_n = D_1/n$ may overestimate the decrease in D upon oligomerization; in this case, the effect (decrease of MFPT upon dimerization/oligomerization) would be stronger than that shown in Figs. 4 and 5.

Close contacts

Model for molecule behavior at a close contact

TCR triggering can be induced by the formation of cellular protrusions called microvilli, which push against a surface, creating a region in close contact (15) between two surfaces, as shown schematically in Fig. 6 *A*. If the close contact membrane separation is smaller than the resting size of CD45, it has been hypothesized that this leads to dynamics in which CD45 can diffuse out but not back into the area of close contact (15). Note that this is distinct from models in which the membrane deformation is tent shaped or wedge shaped, and therefore induces nondiffusive advection on compressed molecules (17). We begin this section by exploring the model regime in which CD45 has an unspecified compressional resistance at a close contact size.

Although the compressional resistance of CD45 is a key property in kinetic segregation models, estimates are challenging. Efforts to measure a similar molecule (49) have yielded estimates around $k_{spring} = 0.1$ p N/nm. If a close contact is held in place by TCRs bound to antigen, the height difference between the rest size of CD45 and the close contact size has been estimated to be $\Delta z = 6.6$ nm (9).

Please cite this article in press as: Taylor et al., Simulation of receptor triggering by kinetic segregation shows role of oligomers and close contacts, Biophysical Journal (2022), https://doi.org/10.1016/j.bpj.2022.03.033

For large regions of close contact, such as those induced by large microvilli, molecular size and compressibility imply an intermediate reentry probability

Using a Boltzmann relationship between the compression energy and the reentry probability (see Methods and Eq. 3), we can compute how these two molecular properties influence the ability of CD45 to enter the close contact shown in Fig. 6 *B*. Stiff or large molecules enter the ROI with near-zero probability, and soft or small molecules enter with high probability, but the physiologically estimated parameters lead to an entry probability of *pentry* entry. Our finding is in contrast to previous models (e.g., (15)), which assumed $pentry = 0$. We perform simulations of the evacuation process with varying *pentry* to investigate its effect on evacuation.

How well approximated is the evacuation time by assuming zero reentry, or by assuming free diffusion? It cannot be well approximated by both, since the evacuation time we found above at $pentry = 1$ is many orders of magnitude larger than the evacuation time in simulations from Fernandes et al. (15), who assumed $pentry = 0$.

Physiological levels of molecular compressibility lead to significant reentry, leading in turn to significant delays in evacuation compared with purely one-way evacuation

We use our WE-Smoldyn algorithm to simulate a density $\rho = 9$ of molecules undergoing diffusion, but with the assumption that a given molecule, after exiting the ROI, reenters with probability *pentry*. We find that the evacuation times, shown in Fig. 6 *C*, indeed vary between the simple diffusion case $pentry = 1$ and the no-entry case *pentry*. The evacuation time, given physiological estimates of k_{spring} and Δz, is around 10^5 s (*pink vertical bar* in Fig. 6 *C*). Although this value is orders of magnitude faster than the evacuation time computed for the $pentry = 1$ case (simple diffusion), it remains substantially longer than T cell triggering times.

Note that estimates of k_{spring} have varied widely (49,50). As empirical uncertainty bounds are not presently available, we explored the effect of a potential twofold increase or decrease of k_{spring}. Propagation of this uncertainty to *pentry* implies a range from 0.36 to 0.77 (*gray dashed lines* in Fig. 6 *C*), with a corresponding variation in the computed MFPT over approximately five orders of magnitude. These results demonstrate the high sensitivity of evacuation times on *pentry* and, in turn, on the biophysical parameters that govern CD45 movement near the close contact.

We validate our results at $pentry = 1$ by comparison with our simulations for simple, unhindered diffusion. We also solve for an analytic expression for the MFPT at $pentry = 0$. This calculation is performed in the supporting material and shown in Fig. S4. Agreement with WE-Smoldyn is shown as the open green circle in Fig. 6 *C*. We further performed brute force simulation for $0 < pentry < 0.3$.

The dramatic effect of even small changes in *pentry* led us to wonder about the relative importance of close contact size and gap size (which determined *pentry*). Note that, so far, all figure panels have shown evacuation time and densities nondimensionalized by scaling with the radius of the ROI. Rescaling to physical units, at a fixed physical density $\tilde{\rho}$, would require simulations over a range of *pentry* and ρ. Instead, we make use of our finding that evacuation time is an approximately exponential function of *pentry*, and use this as an ansatz in Eq. 4 (Methods).

Evacuation times in physical units are shown in Fig. 6 *D*, for a density $160 \times \mu\text{m}^{-2}$. Note that this is lower than the physiological estimates used elsewhere by about fourfold but at the limit of our current computational capability. At these parameters, a close contact region of radius less than ~100 nm evacuates spontaneously in subsecond time. Close contacts that are perfectly impenetrable also evacuate in subsecond time, up to at least 250 nm, comparable with the size observed (15,31). However, close contacts larger than 100 nm with 20% or more reentry probability have significant slow down in evacuation. Here, an observed change in the shape of the curves leads to an interesting prediction: at low $pentry < 0.2$, relative changes in lead to more significant changes in evacuation time compared with the same relative change in close contact radius. At high $pentry > 0.6$, relative changes in close contact radius R_{ROI} lead to more significant changes in evacuation time compared with the same relative change in entry probability. At the physiological estimate $pentry = 0.6$, a roughly 20% reduction in *pentry* has the same effect in reducing MFPT as a roughly 20% reduction in size of the close contact.

DISCUSSION

The paradigm of kinetic segregation—triggering a receptor by local depletion of its deactivating enzyme—has been proposed for a variety of surface receptors (51,52). The most developed example is TCR triggering by CD45 depletion. In this work, we show that, first, simple diffusive motion of CD45 leads to spontaneous depletion extremely rarely, in agreement with previous results (12). Spontaneous depletion is therefore not at risk of false positive receptor triggering in the absence of an external cue. Second, we show that oligomerization of CD45 dramatically increases the speed of depletion. And, third, we show that a close contact may accelerate depletion but, depending on its gap size and the mechanical properties of CD45, depletion may nevertheless be extremely slow.

Our results on oligomerization make a prediction: that externally induced oligomerization of CD45 into higher-order structures would lead to more rapid receptor triggering, and indeed that sufficient oligomerization (e.g., dominant heptamers, Fig. 5) would lead to spontaneous receptor triggering. Such oligomerization could be performed on the extracellular regions of CD45. This could therefore provide

Please cite this article in press as: Taylor et al., Simulation of receptor triggering by kinetic segregation shows role of oligomers and close contacts, Biophysical Journal (2022), https://doi.org/10.1016/j.bpj.2022.03.033

a test of the prediction, particularly in a controlled system, such as a liposomal reconstitution (53). It also predicts a mechanism through which CD45 modulation leads to orders of magnitude changes in a very proximal step in T cell function. It is intriguing to speculate the effect of oligomerization on overall T cell signaling and on engineered T cell function, e.g., T cells used in therapeutics (54,55). However, the observation that CD45 has both positive and negative regulation of overall T cell signaling (13,14,56) suggests a highly nonlinear system, which demands more careful quantitation and quantitative modeling. Outside the context of CD45, galectins (57,58) can cross-link surface proteins via their sugars, but their role is not clear. These galectins can generate higher-order oligomers. They also have weak specificity, and therefore could be a general mechanism to evacuate molecules with many sugars. It could also be that oligomerization is induced not by direct protein-protein interaction, but rather by a mobile raft of lipid heterogeneity. Such oligomers would satisfy a similar mathematical model, perhaps with a different diffusion coefficient.

Calculation of the theoretical evacuation time at a close contact has implications for models of close contact surface molecule dynamics. In particular, Fernandes et al. (15) made the assumption that once a CD45 leaves the close contact region it cannot reenter ($p_{entry} = 0$). We confirm here that this leads to depletion times on the order of seconds. However, using estimates of CD45 geometry and mechanics, we compute that, if there is a 60% chance of reentry, the depletion time increases to 10^5 s, much slower than observed timescales of receptor triggering (15,29,30). Formally, there are several possible resolutions to this discrepancy: if the estimated geometry and mechanical properties of CD45 are accurate, there must be another phenomenon contributing to evacuation. Alternatively, the molecular spacing could be smaller than estimated in (9), or the molecules could be much stiffer. Indeed, according to our model, a factor of two change in the estimate of the latter parameter (i.e., in the spring constant of CD45) induced a greater than 100-fold change in the evacuation time. This sensitivity shows that close contacts under the current model could indeed result in short enough (or nearly so) evacuation times under different estimates of biophysical parameters. Thus, the question of what mechanisms drive evacuation, and particularly the estimation of p_{entry}, warrants further study.

The model we used is minimal in its assumptions and therefore subject to limitations. Our model focuses on the kinetic segregation mechanism; however, it has been proposed that kinetic segregation is just one of many mechanisms contributing to TCR triggering (1). Moreover, we focus on the inhibitory effect of CD45 on TCR signaling, whereas CD45 can both positively and negatively influence TCR signaling (5).

Within the kinetic segregation model, one limitation is our focus exclusively on total depletion, when the last molecule leaves the ROI. In reality, other steps in receptor triggering include ligand binding and receptor phosphorylation (16). So, a more realistic model could be formulated in which the number of CD45 in the ROI determine a next-event rate. This rate would be high for total evacuation, and slower for partial evacuation. The MFPT one would study would be the time until the next event has occurred. Without further assumptions, it is possible this next event could happen slower than the total evacuation time because it adds a subsequent step, or faster, since it can be triggered when evacuation is not total.

Another limitation is the assumption of a flat, 2D membrane. In particular, our consideration of microvilli ignored the purely geometric effect of a microvillus, in which distances around the perimeter of the microvillus are smaller than distances around the ROI in our flat simulations. Simulating diffusion on such curved surfaces is computationally possible, but more expensive, in Smoldyn (44), and would require more characterization of the 3D shape of microvilli.

Yet another limitation is our focus on the motion of CD45, when in reality the receptor moves as well (16). Further integrative models, at the cell scale, may also include multiple receptors, and therefore multiple opportunities for a T cell to activate. Future research may explore these directions.

Crowding is prevalent in biology (59–65). For that reason, there are examples in which *un*-crowding may be important—that is, when molecules must evacuate from a region before a given process can occur, and so the problem of making space is of general interest. These include the many transient cell-cell contacts which occur during tissue development (e.g., the delta-notch system (66,67)). There are also membrane-membrane contacts within cells, including between the endoplasmic reticulum and plasma membrane (where crowding could modulate interactions of molecules including Ora1 and Slim1 (68)). In 1D, an example is offered by transcriptional control in eukaryotes, which is achieved by the binding of many classes of proteins to DNA (69,70). Transcription factors (TFs) locate to binding sites within promoters and enhancers by 1D diffusion along the DNA and by attachment/detachment into the 3D cytoplasm (71–73). The binding of larger structures, such as nucleosomes, which occupy ∼150 basepairs (bp) of DNA, is inhibited by the presence of TFs, and therefore it is intriguing to wonder whether evacuation timescales are significant. Furthermore, enhancers, which are ∼200 bp stretches of DNA with 5–30 TF binding sites of various classes, may require evacuation of nucleosomes and transcriptional repressors to activate their target genes. Again in 1D, microtubules (inflexible polymers of the protein tubulin) are decorated by hundreds of microtubule-associated proteins (74,75). These proteins exhibit significant crowding (62,63) and lateral diffusion along the microtubule lattice (76,77). Large microtubule-binding molecules may therefore have to wait for a region to be clear before binding.

Please cite this article in press as: Taylor et al., Simulation of receptor triggering by kinetic segregation shows role of oligomers and close contacts, Biophysical Journal (2022), https://doi.org/10.1016/j.bpj.2022.03.033

Simulations performed here would be unfeasible without recourse to an enhanced sampling algorithm. WE has been applied to many different types of stochastic dynamics simulations; however, ongoing challenges are present, e.g., in a priori selection of state-space binning strategies, hyperparameters, and weighting schemes to optimize convergence of desired observables (37). Further systematic study of WE hyperparameter selection and analysis methods should lead to further increases in efficiency and empower future rare event simulation studies. Our WE-Smoldyn code base was built on top of the Smoldyn dynamics engine, which is widely used, flexible, and with a large user base. We anticipate the combination of WE with spatial stochastic simulation, as highlighted by full-featured software such as MCell-WESTPA (78), will open new avenues of research, including for the evacuation questions posed in the previous paragraph.

METHODS

Model and dynamics

Diffusion

Smoldyn is a time-stepping simulator with a continuous spatial domain (as opposed to a lattice method). At each time step, molecule displacements are drawn from a Gaussian distribution whose width is determined by their diffusion coefficient D, with each chemical species having their own diffusion coefficient. At each Smoldyn time step, Smoldyn tracks the location of each molecule, and stops when it observes a complete evacuation of the ROI (Fig. 1 *A*, *right*). Aside from interactions with boundaries, barriers, and for molecular binding, all molecules diffuse independently and do not interact with each other. Boundary conditions were chosen to be reflective, although preliminary results did not show substantial differences between reflective and periodic boundary conditions.

As we are using a time-stepping-based method, the determination of whether or not a molecule has evacuated the ROI within a time step is based only on its starting and ending locations, and specific details of the trajectory between the time steps are lost. This representation results in evacuation events that occur between two sequential time steps that are not observed by the method. As evacuation events are lost but none are gained, this would result in estimates of the MFPT that are higher than the true value rather than an underestimate. To minimize the number of evacuation events lost from these missing trajectories, we chose to use a small Smoldyn time step, $\Delta t = 10^{-6}$. To ensure that this choice of Δt is small enough we confirmed that smaller time steps give similar results, as shown in Fig. S2.

Intermolecular interactions and reversible dimerization

Smoldyn uses an algorithm that is qualitatively similar to the Collins-Kimball model of bimolecular reactions and approaches the Smoluchowski model for short time steps (79). The association reaction occurs when two monomers diffuse within a predefined distance of each other, referred to as the binding radius, r_{bind}.

Dissociation of dimers into two monomers is probabilistically determined at each time step, with probability determined by the detachment rate k_{off} (79).

2D reactions are more complicated to analyze than their 3D counterparts (80,81). For example, there is no exact relationship between r_{bind} and a well-mixed k_{on}. We confirm that, for our choice of $\Delta t = 10^{-6}$ and ranges of r_{bind} and k_{off}, the steady-state unbound (monomeric) fraction is a smoothly increasing function of k_{off} and decreasing function of r_{bind}, as shown in Fig. S3 *A*. The dissociation constant, meaning the value of k_{off} at which half of subunits are in monomers, is a weakly increasing function of r_{bind}, as expected by previous theoretical treatments (80,81). The unbinding radius, the distance between two monomers that dissociated in the previous step, was set such that the geminate recombination probability was 0.2, which gives r_{unbind} a nominal value of 0.0443134 ($\approx$4 nm).

Close contacts

By representing close contacts of the system as energy barriers caused by compression of molecules inside the ROI/close contact, we can then model these energy barriers by creating asymmetric behavior between molecules attempting to enter the ROI and those leaving it. Molecules attempting to leave the ROI are free to do so, while those attempting to enter are only allowed to do so probabilistically. The energy barrier between the ROI and rest of the domain is taken to be the energy required to compress a spring, $E_{\text{spring}} = \frac{1}{2} k \Delta z^2$, where k is the physiological spring constant and Δz is the size of the compression. The thermodynamic relationship between this probability and the energy compression is given by

$$pentry = e^{\frac{-E_{\text{spring}}}{k_b T}}, \tag{3}$$

where k_b is Boltzmann's constant and T is the temperature. According to this definition, *pentry* gives the probability that a molecule has energy greater than E_{spring} (and thus may gain entry to the ROI); it follows that *pentry* also equals the ratio of concentrations of molecules inside versus outside the ROI at equilibrium. (Note, however, that *pentry* is not the same as the instantaneous probability of entry of a single molecule during a collision event in the simulation. Particle-based simulation of this type of partial transmission was discussed previously by Andrews (82), and we made use of Smoldyn's built-in functionality for implementation.) In the absence of evidence otherwise, we assume that the presence of the close contact does not influence diffusion coefficient D.

Parameter estimates and model nondimensional scaling

Estimates for R_{ROI} range from 100 to 200 nm (15,17,31), depending in part on the definition, e.g., whether it is the minimum region necessary for receptor triggering, or the observed depletion zone size. The diffusion coefficient D has been estimated to range from 0.01 $\mu\text{m}^2/\text{s}$ (32) to 0.3 $\mu\text{m}^2/\text{s}$ (15). Roughly setting $R_{\text{ROI}} = 100$ nm and $D = 0.01$ $\mu\text{m}^2/\text{s}$ conveniently sets the characteristic timescale $D/R_{\text{ROI}}^2 = 1\text{s}$.

Given the wide ranges of estimates, throughout this work we report times and distances in these scaled (nondimensional) units. Where appropriate, we report results in physical units, denoting these by explicitly including the unit (e.g., s or nm), and, if clarity necessitates, we use a tilde to denote the parameter with physical units. Domain size L and binding radius r_{bind} have units of R_{ROI}. The corresponding physical parameters $\tilde{L} = LR_{\text{ROI}}$ and $\tilde{r}_{\text{bind}} = r_{\text{bind}}R_{\text{ROI}}$ have units of nanometers or microns. The dynamics engine time step Δt has units of D/R_{ROI}^2 and the detachment rate k_{off} has units of R_{ROI}^2/D.

The scaled molecule density ρ has units of molecules per R_{ROI}^2, and the physical molecular density $\tilde{\rho} = \rho/R_{\text{ROI}}^2$ has units of molecules per square nanometer. Another interchangeable quantity is the number of particles in the ROI in a uniform distribution, $\overline{n_{\text{in}}} = \pi\rho = \pi R_{\text{ROI}\rho}^2$. For CD45, estimates range from 482 μm^{-2} (15) to 1000 μm^{-2} (17). For $R_{\text{ROI}} = 100$nm, this corresponds to a density ranging from $\rho = 4.82$ to $\rho = 10$. We use $\rho = 9$ as our focus (17) in all figures unless otherwise noted (e.g., in the ρ sweeps in Fig. 3 and the physical unit plot in Fig. 6 *D*).

Ansatz for rescaling close contact evacuation time to physical units

To return to physical dimensions, a constant physical density $\tilde{\rho}$ requires varying scaled density ρ since $\tilde{\rho} = \rho/R_{\text{ROI}}^2$. In Fig. 6 *D*, we plot the evacuation time in physical units over a range of R_{ROI}. Doing so would require a

Please cite this article in press as: Taylor et al., Simulation of receptor triggering by kinetic segregation shows role of oligomers and close contacts, Biophysical Journal (2022), https://doi.org/10.1016/j.bpj.2022.03.033

full exploration of both nondimensional ρ and *pentry*, which is outside of our computational capacity. So, as an approximation, we take the result in Fig. 6 *C*, which suggests that evacuation time T(*pentry*) is a simple exponential function of *pentry*, that varies between the *pentry* = 0 limit and *pentry* = 1 limit. In other words,

$$T(p) \approx T(0)\left(\frac{T(1)}{T(0)}\right)^{p}, \tag{4}$$

where $p = pentry$. The MFPTs for T(1) can be obtained from the simple diffusion simulations in Fig. 3 *A*, while the MFPTs for T(0) can be obtained analytically, see Fig. S4 *B*.

WE

Algorithm overview

WE obtains information of long timescale processes through multiple short timescale trajectories, hereafter denoted as replicas. A group of simulation replicas are initialized and attributed a probabilistic weight (see Fig. 2 *A*). These replicas are allowed to evolve into a steady-state distribution based on the ensemble space, which is then organized into bins based on location inside the state space. After the definition of these bins, the simulations are allowed to evolve for a fixed amount of time τ with periodic duplication and deletion of certain simulations (Fig. 2 *B*). These duplications and deletions, dubbed splitting and merging, respectively, are done in such a way that preserves the total probabilistic weight of the system: splitting involves separating a simulation into two identical simulations each with half as much weight, and merging involves giving the weight from a deleted simulation to a simulation inside the same bin as the deleted simulation. While the total weight and its distribution between bins might change as the simulation evolves, the number of simulations inside each bin is manipulated so that computation power is evenly split between bins. Our binning order parameter is the number of subunits inside the ROI, n_{in}. So each monomer inside the ROI increased the order parameter by 1, while for simulations with dimerization, each dimer inside the ROI increased the order parameter by 2.

If a replica reached the bin where $n_{in} = 0$, hereafter referred to as the flux bin, the replica is removed from memory, its probabilistic weight is recorded as outgoing flux, and then the weight is redistributed according to one of two different methods (see Fig. S1 and Reweighting methods, below).

Model initialization

Each WE simulation is initialized with 1000 replicas of a Smoldyn simulation. In each replica, each of *N* molecules is randomly and uniformly placed throughout the entire domain. After this initialization, WE splitting and merging and flux measurements are performed before each subsequent step of Smoldyn dynamics (Fig. S1 *C*).

In simulations involving more than one molecular species, initialization is done with homogeneous molecular mixtures; either *N* monomers or *N*/2 dimers are uniformly distributed in the simulation, depending on which is closer to the steady state as found by brute force simulations in Fig. S3.

Reweighting methods

There were two methods of redistributing weight removed from the system through flux into the flux bin ($n_{in} = 0$, see Fig S1). The first method, which was the method used unless otherwise noted, involves redistributing the weight by renormalization; the weight of all remaining replicas is scaled by the total weight remaining in the simulation. If replica *i* evacuates, it is removed and the weight for a replica *j* remaining in the simulation will scale according to

$$w_j \rightarrow \frac{w_j}{1-w_i}. \tag{5}$$

This method works for calculating the mean transition time from the steady-state distribution (or small perturbation from steady state) to a rare fluctuation. In other words, we are measuring the MFPT from $A \rightarrow B$, where *B* is defined as the bin $n_{in} = 0$ (which is rarely visited), and *A* is defined as encompassing all bins $n_{in} \rangle 0$. Note that, in many WE applications, significant time is required for the system to reach steady state, before which accurate MFPT estimates cannot be obtained from the averaged flux-to-target (34). In our system, we know a priori the equilibrium distribution of particles undergoing simple diffusion. Our initialization of replicas according to the equilibrium distribution thus starts close to the nonequilibrium steady-state distribution (reached after some number of τ iterations), where the small weight entering the flux bin is continuously removed and returned to the remaining bins.

In some scenarios, the evacuated state is not rare, and therefore the steady-state distribution is not well approximated by the equilibrium distribution assuming no evacuation. Specifically, this occurs for simple diffusion when $\rho \leq 1$, at the left of Fig. 3 *A*, and for close contact simulations where $pentry \approx 0$ (Fig. 6). In this latter scenario the steady state is the completely evacuated state, and we are seeking to compute a different transition time: from the uniform steady state (as if $pentry = 1$) to the evacuated state. In these scenarios, a second reweighting method was used. This is described schematically in Fig S1 *B*. In these methods, the weight from an evacuated replica is not redistributed to remaining replicas. Rather, each time a replica evacuates, a new replica is initialized as described above and given all of the weight from the evacuating replica. This ensures that the weight distribution throughout the state space remains statistically accurate, even when the flux of weight throughout the space is unidirectional.

Hyperparameters

The above-described WE method requires the specification of hyperparameters τ, m_{targ}, and the max number of iterations. In principle, the selection of these hyperparameters should not impact the results of the WE simulation, but will impact the efficiency of convergence to an accurate MFPT.

In an effort to maximize the observed number of flux events, m_{targ} was chosen to be high to maximize the number of replicas in bins near the flux bin (transient bins), but not higher than allowed by computer memory limitations. The values were $m_{targ} = 100$ for Figs. 3 and S2, and $m_{targ} = 200$ for Figs. 4 and 5.

The WE step was chosen to be $\tau = 50\Delta t$, which we found to be large enough to give replicas time to change bins before the splitting and merging process began, while also avoiding being too long to ensure a high number of replicas inside the transient bins.

Implementation

Smoldyn simulations were executed through Smoldyn's C library, libsmoldyndyn (44). Combination of Smoldyn with WE was written in C and is available to the public at: https://github.com/dydtaylor/LibsmolWE. Execution of libsmoldynWE simulations was done on UCI's high-performance cluster. Brute force Smoldyn simulations were executed in libsmoldyndyn, but outside of the libsmoldynWE weighted ensemble framework. All data were analyzed in MATLAB. Evaluation of analytical solution for $pentry = 1$ was done in Wolfram Mathematica.

Analysis

To allot for burn-in time, i.e., an initial transient while the replicas approach a steady state, the first half of each run is discarded, and the mean flux measured in the second half of the run is taken to be a single measurement of the mean flux $\overline{\varphi}$, averaged across WE steps. Each WE data point in this paper is calculated from 10 independent WE simulations; multiple independent runs are used to minimize the effect of spurious correlations between iterations (37), which can cause interrun variability in estimates (e.g., as seen in Fig. 2 *C*). These 10 repeats are then arithmetically averaged to give an estimate of the mean flux, averaged across repeats, $\langle\overline{\varphi}\rangle$, with error bars given by the standard error of the mean for the 10 WE simulations.

Please cite this article in press as: Taylor et al., Simulation of receptor triggering by kinetic segregation shows role of oligomers and close contacts, Biophysical Journal (2022), https://doi.org/10.1016/j.bpj.2022.03.033

The average flux recorded from replicas reaching the flux bin, $\overline{\varphi}$, is used to calculate the MFPT from the Hill relation (34,83), $T = 1/\overline{\varphi}$. The error bars of the flux $\delta\varphi$ then propagate to MFPT error bars by $\delta T = |T|^2\delta\varphi$.

To calculate MFPT from brute force simulations, the arithmetic mean of 1000 (Fig. 3) or 500 (Fig. S4 *B*) independent repeats was used, with error bars giving the standard error of the mean for those simulations. To calculate the single molecule first passage time distribution for Fig. S4 *A*, an empirical CDF was created from the result of 20,000 brute force evacuations of a single molecule placed uniformly within the ROI.

To calculate monomer fractions from brute force simulations, purely monomeric Smoldyn simulations are initialized and run for 15 units of time. Afterward, the monomer fraction we report is average measured over these last 5 time units.

Method validation

Several methods were used to validate the WE results. For MFPTs where achieving brute force results was computationally viable, brute force results were included along with WE results (see Figs. 3 and 6 *C*). Monomer and dimer fractions were verified with brute force Smoldyn simulations (Fig. S3).

For each binding radius presented, the sigmoidal monomer fraction versus unbinding rate curve was executed for a range of time steps to verify that the time step of $\Delta t = 10^{-2}$ was small enough.

Close contact WE simulations were found to agree with brute force simulations for low *pentry* (Fig. 6 *C*). For $pentry = 1$ we verified the endpoint with our simple diffusion WE simulations for $\rho = 9$.

An analytical solution for close contact simulations when $pentry = 0$ was obtained, see supporting material. The analytic solution for a single molecule's first passage time distribution was compared with an empirical CDF obtained from 20,000 brute force Smoldyn simulations (Fig. S4 *A*) and the analytical form for the MFPT for a variety of evacuating molecules was compared with the results from brute force Smoldyn simulations, 500 for each data point (Fig. S4 *B*). The analytic solution for the parameters used in the close contact WE simulations is included in Fig. 6 *C*.

An asymptotic solution for the MFPT for homogeneous monomeric solutions was obtained from previous work (12). When applicable, these asymptotics were used to verify WE results (Figs. 3 *A* and S2).

However, as can be seen in Figs. 3 and S2, agreement with the asymptotics at higher densities is dependent on the size of the domain used. For a range of densities, we did a sweep of domain sizes (Fig. S2). WE estimates reach to within one order of magnitude of the asymptotics above $\approx L = 5$ at the highest simulated densities.

Convergence in time steps was done by comparing MFPT estimates for larger time steps with the chosen time step to ensure that MFPT estimates did not undergo drastic differences in MFPT estimates. The time step of $\Delta t = 10^{-6}$, used for all simulations unless otherwise stated, is compared with the time step of $\Delta t = 5 \times 10^{-6}$ shown in Figs. S2B–S3D.

SUPPORTING MATERIAL

Supporting material can be found online at https://doi.org/10.1016/j.bpj.2022.03.033.

AUTHOR CONTRIBUTIONS

J.A. and E.L.R. designed the research. R.T. developed code, performed research, and analyzed data. R.T., J.A., and E.L.R. wrote the manuscript.

ACKNOWLEDGMENTS

We thank Omer Dushek (Oxford), Jay Newby (U Alberta), Brian Chu (UC Irvine), and Dhiman Ray (UC Irvine) for valuable discussion. This work was supported by: NSF grant DMS 1715455to E.L.R.; NSF CAREER grant DMS 1454739 to J.A.; NSF grant DMS 1763272; and a grant from the Simons Foundation (594598, QN).

REFERENCES

1. van der Merwe, P. A., and O. Dushek. 2011. Mechanisms for T cell receptor triggering. *Nat. Rev. Immunol.* 11:47–55.
2. Siller-Farfán, J. A., and O. Dushek. 2018. Molecular mechanisms of T cell sensitivity to antigen. *Immunol. Rev.* 285:194–205.
3. Lin, J., and A. Weiss. 2003. The tyrosine phosphatase CD148 is excluded from the immunologic synapse and down-regulates prolonged T cell signaling. *J. Cell Biol.* 162:673–682.
4. Varma, R., G. Campi, …, M. L. Dustin. 2006. T cell receptor-proximal signals are sustained in peripheral microclusters and terminated in the central supramolecular activation cluster. *Immunity.* 25:117–127.
5. Courtney, A. H., A. A. Shvets, …, A. Weiss. 2019. CD45 functions as a signaling gatekeeper in T cells. *Sci. Signaling.* 12:eaaw8151.
6. Razvag, Y., Y. Neve-Oz, …, E. Sherman. 2019. T cell activation through isolated tight contacts. *Cell Rep.* 29:3506–3521.e6.
7. Carbone, C. B., N. Kern, …, R. D. Vale. 2017. In vitro reconstitution of T cell receptor-mediated segregation of the CD45 phosphatase. *Proc. Natl. Acad. Sci. U S A.* 114:E9338–E9345.
8. Felce, J. H., E. Sezgin, …, S. J. Davis. 2018. CD45 exclusion– and cross-linking–based receptor signaling together broaden FcεRI reactivity. *Sci. Signaling.* 11:eaat0756.
9. Chang, V. T., R. A. Fernandes, …, S. J. Davis. 2016. Initiation of T cell signaling by CD45 segregation at close contacts. *Nat. Immunol.* 17:574.
10. Choudhuri, K., D. Wiseman, …, P. A. van der Merwe. 2005. T-cell receptor triggering is critically dependent on the dimensions of its peptide-MHC ligand. *Nature.* 436:578–582.
11. Jung, Y., I. Riven, …, G. Haran. 2016. Three-dimensional localization of T-cell receptors in relation to microvilli using a combination of superresolution microscopies. *Proc. Natl. Acad. Sci. U S A.* 113:E5916–E5924.
12. Newby, J., and J. Allard. 2016. First-passage time to clear the way for receptor-ligand binding in a crowded environment. *Phys. Rev. Lett.* 116:128101.
13. Takeda, A., A. Matsuda, …, N. R. Yaseen. 2004. CD45-associated protein inhibits CD45 dimerization and up-regulates its protein tyrosine phosphatase activity. *Blood.* 103:3440–3447.
14. Xu, Z., and A. Weiss. 2002. Negative regulation of CD45 by differential homodimerization of the alternatively spliced isoforms. *Nat. Immunol.* 3:764–771.
15. Fernandes, R. A., K. A. Ganzinger, …, D. Klenerman. 2019. A cell topography-based mechanism for ligand discrimination by the T cell receptor. *Proc. Natl. Acad. Sci. U S A.* 116:14002–14010.
16. Chen, K. Y., E. Jenkins, …, S. J. Davis. 2021. Trapping or slowing the diffusion of T cell receptors at close contacts initiates T cell signaling. *Proc. Natl. Acad. Sci. U S A.* 118, e2024250118.
17. Allard, J. F., O. Dushek, …, P. A. van der Merwe. 2012. Mechanical modulation of receptor-ligand interactions at cell-cell interfaces. *Biophys. J.* 102:1265–1273.
18. Pullen, R. H., and S. M. Abel. 2017. Catch bonds at T cell interfaces: impact of surface reorganization and membrane fluctuations. *Biophys. J.* 113:120–131.
19. Fujiwara, T. K., K. Iwasawa, …, A. Kusumi. 2016. Confined diffusion of transmembrane proteins and lipids induced by the same actin meshwork lining the plasma membrane. *Mol. Biol. Cell.* 27:1101–1119.
20. Shi, X., Y. Bi, …, C. Xu. 2014. Ca2+ regulates T-cell receptor activation by modulating the charge property of lipids. *Nature.* 493:111.
21. Rajani, V., G. Carrero, …, C. Cairo. 2011. Analysis of molecular diffusion by first-passage time variance identifies the size of confinement zones. *Biophys. J.* 100:1463–1472.

22. Ma, Y., Y. J. Lim, …, K. Gaus. 2020. Clustering of the ζ-chain can initiate T cell receptor signaling. *Int. J. Mol. Sci.* 21:3498.
23. Connolly, A., R. Panes, …, E. Gagnon. 2021. TMEM16F mediates bystander TCR-CD3 membrane dissociation at the immunological synapse and potentiates T cell activation. *Sci. Signaling.* 14:eabb5146.
24. Clemens, L., O. Dushek, and J. Allard. 2021. Intrinsic disorder in the T cell receptor creates cooperativity and controls ZAP70 binding. *Biophys. J.* 120:379–392.
25. Li, Q.-J., A. R. Dinner, …, A. K. Chakraborty. 2004. CD4 enhances T cell sensitivity to antigen by coordinating Lck accumulation at the immunological synapse. *Nat. Immunol.* 5:791–799.
26. Lin, H., and J. Wooley. 2005. Computational modeling and simulation as enablers for biological discovery. *In* Catalyzing Inquiry at the Interface of Computing and Biology. J. C. Wooley and H. S. Lin, eds. National Academies Press (US), p. 468.
27. Huber, G. A., and S. Kim. 1996. Weighted-ensemble Brownian dynamics simulations for protein association reactions. *Biophys. J.* 70:97–110.
28. Goswami, D., K. Gowrishankar, …, S. Mayor. 2008. Nanoclusters of GPI-anchored proteins are formed by cortical actin-driven activity. *Cell.* 135:1085–1097.
29. Irvine, D. J., M. A. Purbhoo, …, M. M. Davis. 2002. Direct observation of ligand recognition by T cells. *Nature.* 419:845–849.
30. Huang, J., M. Brameshuber, …, M. M. Davis. 2013. A single peptide-major histocompatibility complex ligand triggers digital cytokine secretion in CD4+ T cells. *Immunity.* 39:846–857.
31. Cai, E., K. Marchuk, …, M. F. Krummel. 2017. Visualizing dynamic microvillar search and stabilization during ligand detection by T cells. *Science.* 356:eaal3118.
32. Cairo, C. W., R. Das, …, D. E. Golan. 2010. Dynamic regulation of CD45 lateral mobility by the spectrin-ankyrin cytoskeleton of T cells. *J. Biol. Chem.* 285:11392–11401.
33. Andrews, S. S., N. J. Addy, …, A. P. Arkin. 2010. Detailed simulations of cell biology with Smoldyn 2.1. *PLoS Comput. Biol.* 6:e1000705.
34. Bhatt, D., B. W. Zhang, and D. M. Zuckerman. 2010. Steady-state simulations using weighted ensemble path sampling. *J. Chem. Phys.* 133:014110.
35. Zhang, B. W., D. Jasnow, and D. M. Zuckerman. 2010. The "weighted ensemble" path sampling method is statistically exact for a broad class of stochastic processes and binning procedures. *J. Chem. Phys.* 132:54107.
36. Donovan, R. M., A. J. Sedgewick, …, D. M. Zuckerman. 2013. Efficient stochastic simulation of chemical kinetics networks using a weighted ensemble of trajectories. *J. Chem. Phys.* 139:115105.
37. Zuckerman, D. M., and L. T. Chong. 2017. Weighted ensemble simulation: review of methodology, applications, and software. *Annu. Rev. Biophys.* 46:43–57.
38. Cytrynbaum, E. N., Y. D. Li, …, H. Mehrabian. 2012. Estimating the bending modulus of a FtsZ bacterial-division protein filament. *Phys. Rev. E.* 85:011902.
39. Wu, Y., J. Vendome, …, B. Honig. 2011. Transforming binding affinities from three dimensions to two with application to cadherin clustering. *Nature.* 475:510–513.
40. Johnson, M. E., A. Chen, …, A. M. Uhrmacher. 2021. Quantifying the roles of space and stochasticity in computer simulations for cell biology and cellular biochemistry. *Mol. Biol. Cell.* 32:186–210.
41. Yogurtcu, O. N., and M. E. Johnson. 2018. Cytosolic proteins can exploit membrane localization to trigger functional assembly. *Plos Comput. Biol.* 14:e1006031.
42. Bell, G., M. Dembo, and P. Bongrand. 1984. Cell adhesion. competition between nonspecific repulsion and specific bonding. *Biophys. J.* 45:1051–1064.
43. Huppa, J. B., M. Axmann, …, M. M. Davis. 2010. TCR–peptide–MHC interactions in situ show accelerated kinetics and increased affinity. *Nature.* 463:963–967.
44. Andrews, S. S. 2017. Smoldyn: particle-based simulation with rule-based modeling, improved molecular interaction and a library interface. *Bioinformatics.* 33:710–717.
45. Andrews, S. S. 2019. Modeling biomolecular site dynamics, methods and protocols. *Methods Mol. Biol. (N. Y.).* 1945:179–202.
46. Gambin, Y., R. Lopez-Esparza, …, W. Urbach. 2006. Lateral mobility of proteins in liquid membranes revisited. *Proc. Natl. Acad. Sci. U S A.* 103:2098–2102.
47. Ramadurai, S., A. Holt, …, B. Poolma n. 2009. Lateral diffusion of membrane proteins. *J. Am. Chem. Soc.* 131:12650–12656, PMID: 19673517.
48. Javanainen, M., H. Martinez-Seara, …, I. Vattulainen. 2017. Diffusion of integral membrane proteins in protein-rich membranes. *J. Phys. Chem. Lett.* 8:4308–4313, PMID: 28823153.
49. Burroughs, N. J., K. Köhler, …, D. M. Davis. 2011. Boltzmann energy-based image analysis demonstrates that extracellular domain size differences explain protein segregation at immune synapses. *Plos Comput. Biol.* 7:e1002076.
50. Burroughs, N. J., and C. Wülfing. 2002. Differential segregation in a cell-cell contact interface: the dynamics of the immunological synapse. *Biophys. J.* 83:1784–1796.
51. Dushek, O., J. Goyette, and P. A. Van Der Merwe. 2012. Non-catalytic tyrosine-phosphorylated receptors. *Immunol. Rev.* 250:258–276.
52. Natkanski, E., W. Y. Lee, …, P. Tolar. 2013. B Cell use mech. energ. discriminate antigen affinities. *Science (New York, NY).* 340:1587–1590.
53. Hui, E. 2019. Understanding T cell signaling using membrane reconstitution. *Immunol. Rev.* 291:44–56.
54. Harris, M. J., M. Fuyal, and J. R. James. 2021. Quantifying persistence in the T-cell signaling network using an optically controllable antigen receptor. *Mol. Syst. Biol.* 17:e10091.
55. Waldman, A. D., J. M. Fritz, and M. J. Lenardo. 2020. A guide to cancer immunotherapy: from T cell basic science to clinical practice. *Nat. Rev. Immunol.* 20:651–668.
56. Furlan, G., T. Minowa, …, Y. Kaizuka. 2014. Phosphatase CD45 both positively and negatively regulates T cell receptor phosphorylation in reconstituted membrane protein clusters. *J. Biol. Chem.* 289:28514–28525.
57. Farhadi, S. A., R. Liu, …, G. A. Hudalla. 2021. Physical tuning of galectin-3 signaling. *Proc. Natl. Acad. Sci. U S A.* 118, e2024117118.
58. Farhadi, S., R. Liu, and G. Hudalla. 2021. Tuning multivalent signaling of extracellular galectin-3. *FASEB J.* 35:03143.
59. Candotti, M., and M. Orozco. 2016. The differential response of proteins to macromolecular crowding. *Plos Comput. Biol.* 12:e1005040.
60. Elcock, A. H. 2010. Models of macromolecular crowding effects and the need for quantitative comparisons with experiment. *Curr. Opin. Struct. Biol.* 20:196–206.
61. Dyson, L., and R. E. Baker. 2015. The importance of volume exclusion in modelling cellular migration. *J. Math. Biol.* 71:1–21.
62. Conway, L., D. Wood, …, J. L. Ross. 2012. Motor transport of self-assembled cargos in crowded environments. *Proc. Natl. Acad. Sci. U S A.* 109:20814–20819.
63. Leduc, C., K. Padberg-Gehle, …, J. Howard. 2012. Molecular crowding creates traffic jams of kinesin motors on microtubules. *Proc. Natl. Acad. Sci. U S A.* 109:6100–6105.
64. Stachowiak, J. C., E. M. Schmid, …, C. C. Hayden. 2012. Membrane bending by protein–protein crowding. *Nat. Cell Biol.* 14:944–949.
65. Mcguffee, S. R., and A. H. Elcock. 2010. Diffusion, crowding & protein stability in a dynamic molecular model of the bacterial cytoplasm. *Plos Comput. Biol.* 6:e1000694.
66. Meloty-Kapella, L., B. Shergill, …, G. Weinmaster. 2012. Notch ligand endocytosis generates mechanical pulling force dependent on dynamin, epsins, and actin. *Dev. Cell.* 22:1299–1312.

67. Shergill, B., L. Meloty-Kapella, …, E. Botvinick. 2012. Optical tweezers studies on notch: single-molecule interaction strength is independent of ligand endocytosis. *Dev. Cell.* 22:1313–1320.

68. Li, L., X. Shi, …, C. Xu. 2014. Ionic protein–lipid interaction at the plasma membrane: what can the charge do? *Trends Biochem. Sci.* 39:130–140.

69. Sneppen, K., M. A. Micheelsen, and I. B. Dodd. 2008. Ultrasensitive gene regulation by positive feedback loops in nucleosome modification. *Mol. Syst. Biol.* 4:1–5.

70. Kepler, T. B., and T. C. Elston. 2001. Stochasticity in transcriptional regulation: origins, consequences, and mathematical representations. *Biophys. J.* 81:3116–3136.

71. Hammar, P., P. Leroy, …, J. Elf. 2012. The Lac Repressor displays facilitated diffusion in living cells. *Science (New York, NY).* 336:1595–1598.

72. McKinney, K., M. Mattia, …, C. Prives. 2004. p53 linear diffusion along DNA requires its C terminus. *Mol. Cell.* 16:413–424.

73. Mirny, L., M. Slutsky, …, A. Kosmrlj. 2009. How a protein searches for its site on DNA: the mechanism of facilitated diffusion. *J. Phys. A: Math. Theor.* 42:434013.

74. Alberts, B., A. Johnson, K. Roberts…, 2014. Molecular Biology of the Cell. Garland, New York.

75. Rouzier, R., R. Rajan, …, L. Pusztai. 2005. Microtubule-associated protein tau: a marker of paclitaxel sensitivity in breast cancer. *Proc. Natl. Acad. Sci. U S A.* 102:8315–8320.

76. Dixit, R., J. L. Ross, …, E. L. F. Holzbaur. 2008. Differential Regul. Dynein Kinesin Mot. Proteins by Tau. *Science (New York, NY).* 319:1086–1089.

77. Helenius, J., G. Brouhard, …, J. Howard. 2006. The depolymerizing kinesin MCAK uses lattice diffusion to rapidly target microtubule ends. *Nature.* 441:115–119.

78. Donovan, R. M., J.-J. Tapia, …, D. M. Zuckerman. 2016. Unbiased rare event sampling in spatial stochastic systems biology models using a weighted ensemble of trajectories. *PLoS Comput. Biol.* 12:e1004611.

79. Bray, S. S. A., and A. Dennis. 2004. Stochastic simulation of chemical reactions with spatial resolution and single molecule detail. *Phys. Biol.* 1:137.

80. Yogurtcu, O. N., and M. E. Johnson. 2015. Theory of bi-molecular association dynamics in 2D for accurate model and experimental parameterization of binding rates. *J. Chem. Phys.* 143:08B614_1.

81. Lawley, S. D., and J. P. Keener. 2017. Rebinding in biochemical reactions on membranes. *Phys. Biol.* 14:56002.

82. Andrews, S. S. 2009. Accurate particle-based simulation of adsorption, desorption and partial transmission. *Phys. Biol.* 6:046015.

83. Hill, Terrell L. 1989. Free Energy Transduction and Biochemical Cycle Kinetics. Springer-Verlag, New York.